Joule

Article

Cross-plane iridium-based filaments sap efficiency in proton exchange membrane electrolyzers

Graphical abstract

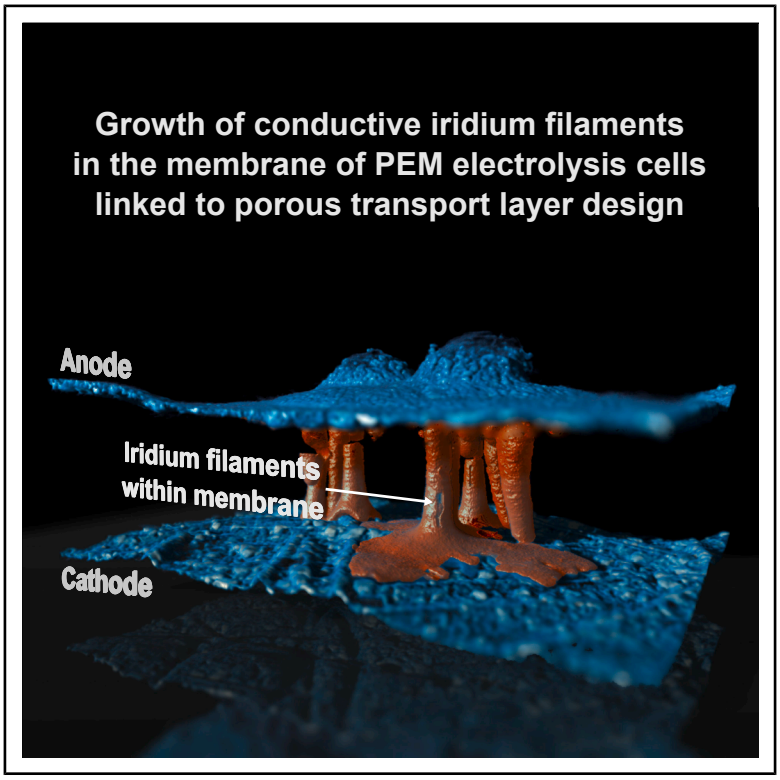

Authors

Christine Heume, Violeta Karyofylli, Ali Javed, ..., André Karl, Günter Schmid, Rüdiger-A. Eichel

Correspondence

ch.heume@fz-juelich.de

In brief

This study reveals that conductive iridium filaments can form across the membrane in proton exchange membrane electrolyzers, creating parasitic current pathways and reducing system efficiency. The findings link filament formation to porous transport layer design, providing insights to improve the durability and lifetime of industrial water electrolyzers.

Highlights

- Parasitic current pathways from iridium filament growth within the membrane
- Catalyst migration initiated beneath porous transport layer weld seams
- Aging revealed after long-term electrolyzer operation
- Insights for improving durability and efficiency of water electrolyzers

Heume et al., 2026, Joule *10*, 102238
February 18, 2026
https://doi.org/10.1016/j.joule.2025.102238

CellPress

Joule

CellPress
OPEN ACCESS

Article

Cross-plane iridium-based filaments sap efficiency in proton exchange membrane electrolyzers

Christine Heume,[1,2,6,*] Violeta Karyofylli,[1] Ali Javed,[1] Krzysztof Dzieciol,[1] Shibabrata Basak,[1] Jean-Pierre Poc,[1,2] Yasemin Tasdemir,[1] Yannik Rutsch,[1,2] Lukas Rein,[1,2] Niklas Wolf,[1,2] Sebastian Speer,[1,2] Sven Jovanovic,[1] Leander Treutlein,[1,2] Julian Borowec,[1,2] Florian Hausen,[1,2] Ladislaus Dobrenizki,[4] Stephan Malmberg,[4] Josef Granwehr,[1,5] Hans Kungl,[1] Eva Jodat,[1] Peter Geskes,[4] André Karl,[1] Günter Schmid,[4] and Rüdiger-A. Eichel[1,2,3]

[1]Institute of Energy Technologies – Fundamental Electrochemistry (IET-1), Forschungszentrum Jülich GmbH, 52428 Jülich, Germany

[2]Institute of Physical Chemistry, RWTH Aachen University, 52074 Aachen, Germany

[3]Faculty of Mechanical Engineering, RWTH Aachen University, 52074 Aachen, Germany

[4]Siemens Energy Global GmbH & Co. KG, Transformation of Industry – Sustainable Energy Systems – Product Management, 91058 Erlangen, Germany

[5]Institute of Technical and Macromolecular Chemistry, RWTH Aachen University, 52074 Aachen, Germany

[6]Lead contact

*Correspondence: ch.heume@fz-juelich.de

https://doi.org/10.1016/j.joule.2025.102238

CONTEXT & SCALE Proton exchange membrane electrolysis cells (PEMECs) are a key technology for producing green hydrogen at high purity and efficiency. As the hydrogen economy expands, PEMECs must operate reliably for tens of thousands of hours under industrial conditions. However, understanding aging and degradation modes at this scale remains limited, hindering the development of predictive lifetime models and robust cell designs.

This study reports a newly recognized aging phenomenon in PEMECs operated under realistic, industrially relevant conditions for 5,000 h. Using advanced analytical methods, we identify the formation of iridium filaments that grow across the membrane, creating parasitic current pathways that reduce system efficiency. These filaments originate beneath weld seams in the anodic porous transport layer (PTL), where local mechanical and electrical inhomogeneities enhance current density and promote catalyst dissolution and migration.

The discovery of filament formation and its mechanistic link to PTL structure provides a new perspective on material interactions within operating electrolyzers. These insights offer practical guidance for designing more stable components and mitigating degradation, which is critical for extending electrolyzer lifetime, reducing hydrogen production costs, and supporting the large-scale deployment of renewable energy systems.

SUMMARY

Proton exchange membrane electrolysis cells (PEMECs) are key to producing green hydrogen. The success of the green hydrogen economy depends on the technical maturity and scalability of water electrolysis systems. However, achieving energy-efficient and long-term operation requires a thorough understanding of aging mechanisms. While PEMECs have been extensively studied under laboratory conditions, data derived from industrial-scale operations are scarce.

Our study addresses aging in an industry-oriented PEMEC operated under realistic conditions for 5,000 h, revealing systematic parasitic current pathways from cross-plane iridium filaments within the membrane, correlated with the anode/porous transport layer (PTL) interface. Experiments and computational models confirm that these parasitic currents do not impede system operation but do reduce system efficiency. This filament formation associated with the anode/PTL interface represents a hitherto unreported source of aging within PEMECs. Our findings will help optimize PEMEC design, effectively improving system performance and lifetime on an industrial scale, thus advancing the green hydrogen economy.

INTRODUCTION

Green hydrogen, produced in an environmentally sustainable way using renewable resources, is a key energy carrier for driving our future global energy economy. Additionally, it can be exploited to synthesize other platform chemicals for manufacturing a plethora of valuable chemicals whose large-scale production had mostly relied on fossil resources. In core industrial sectors, often termed "hard-to-abate" because they cannot be directly electrified, green hydrogen is therefore crucial to attain climate neutrality. How fast a green hydrogen economy can be ramped up, however, poses a major challenge and depends critically on the technical maturity of water electrolysis—the most energy-consuming step, which determines the economic viability of green hydrogen value chains.[1,2]

To anchor investment in a green energy economy on a solid footing,[3] it is pivotal to scale up and develop water electrolysis to a high level of technological maturity that ensures its energy-efficient and long-term operation. This requires thoroughly de-risking the technology itself on every level.[4] A key task of the de-risking process is to understand aging and degradation phenomena qualitatively[5] and to set up robust quantitative models to predict performance variation for a given system design and operation strategy. Comprehensively understanding such phenomena is essential for developing mitigation measures. Thus, de-risking proton exchange membrane electrolyzer cells (PEMEC), one of the most promising water electrolysis technologies, is a decisive task for research and development, paving the way to a green hydrogen economy.[6,7]

While PEMECs have been studied extensively on a laboratory scale[8,9] with idealized load profiles, studies on an industrially relevant scale are rare.[9–12] Laboratory-scale findings point to a complex interplay between the various electrolyzer components, such as the catalyst layer (CL), membrane electrode assembly (MEA), porous transport layer (PTL), and bipolar plate (BPP), but also the applied operation profile.[13–15] On an atomic level, instabilities are mainly associated with the typically iridium-based oxygen evolution reaction (OER) catalysts.[16–20] Another key driver for PEMEC degradation is the chemical and mechanical instability, presumably induced by external impurities, of perfluorosulfonic acid (PFSA) membranes.[21,22] Yet one should be cautious about applying laboratory-scale-derived data to draw conclusions about industrially relevant systems. Even so, understanding the mechanisms of microstructural features and corresponding internal resistances, which may impair charge transport, is important for advancing the performance and durability of PEMEC. Now, for the first time, realistic "test field data" were available in the flagship project DERIEL (de-risking PEM electrolyzer) of the German H_2Giga initiative.[23] The investigations within the DERIEL project cover a spectrum ranging from small individual laboratory cells to application-oriented test stations in the kilo- and megawatt range (see Figure 1), including the selection and definition of suitable operating windows and protocols for special operating conditions, such as start/stop, load change, or emergency shutdown. This gave us the unique opportunity to develop a fundamental understanding of the underlying processes of aging, failure, and degradation modes. These insights are key to optimizing the entire system according to the Pareto principle in a time- and cost-effective manner. The durability test runs of 5,000 h included 155 start-stop cycles according to the arbitrary net profile at the given time period of the test.

This study aims to elucidate aging phenomena in MEAs from a PEMEC by multi-modal comparison between pristine and post-operated and aged samples. In particular, samples from MEAs from several experiments that exhibited early signs of parasitic current pathways through the membrane were selected for further study. These pathways can contribute to parasitic currents that are defined as electrical currents, which occur below the open-circuit voltage (OCV) of the electrolysis cell and thus do not impede safe system operation.[24] The samples had been cycled in systems employing expanded metal meshes as a cost-efficient alternative to purpose-machined flow fields in the BPP.[25–27] During the fabrication of such metal meshes, weld seams are formed in the PTL. Consequently, the MEA and PTL interface is expected to be non-uniform, which, in turn, may lead to local field enhancement patterns, inhomogeneous current density distributions, or mechanical damage in the MEA. By approximating a realistic industrial system design, previously unobserved aging phenomena might be detected and subsequently eliminated, both being essential for the de-risking process of PEMEC systems.

RESULTS AND DISCUSSION

Parasitic currents and gas crossover post-operation

Industrial-scale electrolyzer systems typically consist of megawatt-scale stack arrays. The stacks, in turn, contain multiple electrolysis cells, where the individual performance is characterized by polarization curves. Particularly, the shape of the curve above the water decomposition voltage of 1.23 V provides information about the overvoltage, and the slope of the curve below the decomposition voltage gives information about possible leakage currents.[28] An initial comparison between pristine and post-operated MEAs (Figure 2A) shows a similar shape above the decomposition voltage at current densities ranging from 4 mA/cm^2 to 1 A/cm^2. However, in the very low current density range from 0.1 to 4 mA/cm^2, below the decomposition voltage, the post-operated MEA exhibits a markedly decreased slope, a clear indication of a parasitic current pathway.[29] Despite the cross-plane nature of the parasitic current, the invariant shape of the polarization curve at higher currents points to a continuous operation of the electrolyzer.

First, the hydrogen permeability of both MEAs was studied to investigate if the measured parasitic current was caused by gas leakage (Figure 2B). In general, given that the majority of gas crossover occurs in the aqueous phase,[30] the hydrogen gas permeability of the dry MEAs is lower than that of the wet MEAs. However, the post-operated MEA shows a higher hydrogen permeability in both the dry and wet states, contradicting the typical behavior documented in literature for used PFSA membranes, in which an increase in crystallinity and equivalent weight should result in decreased permeability.[31,32]

Given the observation of both parasitic current and increased hydrogen gas crossover in the post-operated MEA, a dedicated electrochemical computational model was developed

Figure 1. Test field environment used in DERIEL MW stack test bench (left) and kW stack test benches (right) (copyright by Siemens Energy)

to investigate their impact on electrolyzer performance. For this, a one-dimensional model was used to describe stationary and isothermal transport processes.[33–35] In Figures 2C and 2D, the considered transport phenomena are schematically summarized, and the most crucial ones for each scenario are highlighted within boxes. A detailed description of the model can be found in the work of Karyofylli et al.[36] In the first scenario the dependence of the polarization behavior on the electron conductivity across the membrane was tested (Figure 2C), while the second computational scenario focused on investigating the impact of gas crossover (Figure 2D). A strong impact on the polarization curve is predicted by the theoretical model when the overall electronic conductivity through the membrane rises above 1.0×10^{-1} S/cm, consistent with the observed behavior in the measured polarization curves (Figure 2A). Similarly, in another study,[29] current flow was observed in a cell at voltages below the OCV, which was attributed to potential membrane rupture and parasitic currents within the membrane, resulting from extended operation at high current densities. Since the measured polarization curve of the post-operated MEA in Figure 2A depicts similar shifts in the current density, our model hints at the existence of parasitic current pathways. By contrast, for the increased gas-crossover scenario, only small increases in the overpotential are predicted by the model, even at high gas-crossover values. This suggests that slight increases in gas permeation alone cannot explain the observed polarization behavior. To further assess the impact of these phenomena, the Faradaic efficiency (η_{H2}) of hydrogen production was also estimated computationally. Concurring with literature,[29,37] both high values for gas permeation and cross-membrane current pathways strongly affect the Faradaic efficiency. This underscores the severe effect that both gas crossover and parasitic currents can have on the hydrogen production efficiency most prominently observed at low load regime. Consequently, understanding their origin and inhibition is paramount for operating industrial-scale electrolyzers when considering the levelized cost of hydrogen production.

XCT and FIB-SEM investigation

Based on the results of the electrochemical characterization in conjunction with the computational model, morphological changes of the post-operated membrane were suspected and, thus, were investigated using a multi-modal approach.

First, X-ray computed tomography (XCT) was applied, allowing the non-invasive imaging of the MEAs. The XCT measurements of the MEA in its pristine state show no anomalies (Figure S1). By contrast, through-plane projections of post-operated MEAs exhibit a repetitive pattern of high-intensity voxels spaced approximately 2 mm apart (Figure 3A), correlating precisely to the positions of weld seams in the expanded metal PTL applied at the anode during operation (Figures 3B–3D). Each high-intensity spot corresponds to a cluster of structures within the membrane (Figure 3C). As the X-ray attenuation increases with atomic number,[39] the strong contrast between these structures and the surrounding membrane implies that they consist of a material with significantly higher density and are therefore likely migrated catalyst material. To gain more detailed insight, the structures were examined at higher magnification. Figure 3E shows a single slice of the tomogram, while Figure 3F displays the projection of the maximal intensity of all slices, highlighting multiple distinct features within the membrane. Specifically, each bright spot observed on the overview tomograms (Figure 3A) corresponds to a cluster of filament-like formations, hereafter referred to as "filaments." Besides the filaments, bulges on the anode can be observed. Each bulge is approximately 50 μm high and shows missing catalyst material on top (Figure 3E). Directly beneath the anode, surrounding the filaments, droplet-like structures can be observed (Figure 3E). These structures indicate that the filament growth initiates from the anode and extends toward the cathode. However, upon reaching the cathode, the filaments begin to disperse—spreading like a pancake—at the cathode interface, as is shown in the three-dimensional segmentation in Figure 3H. Investigations of similar samples with a shorter runtime of 1,200 h show partially developed filaments (Figure 3G), supporting the

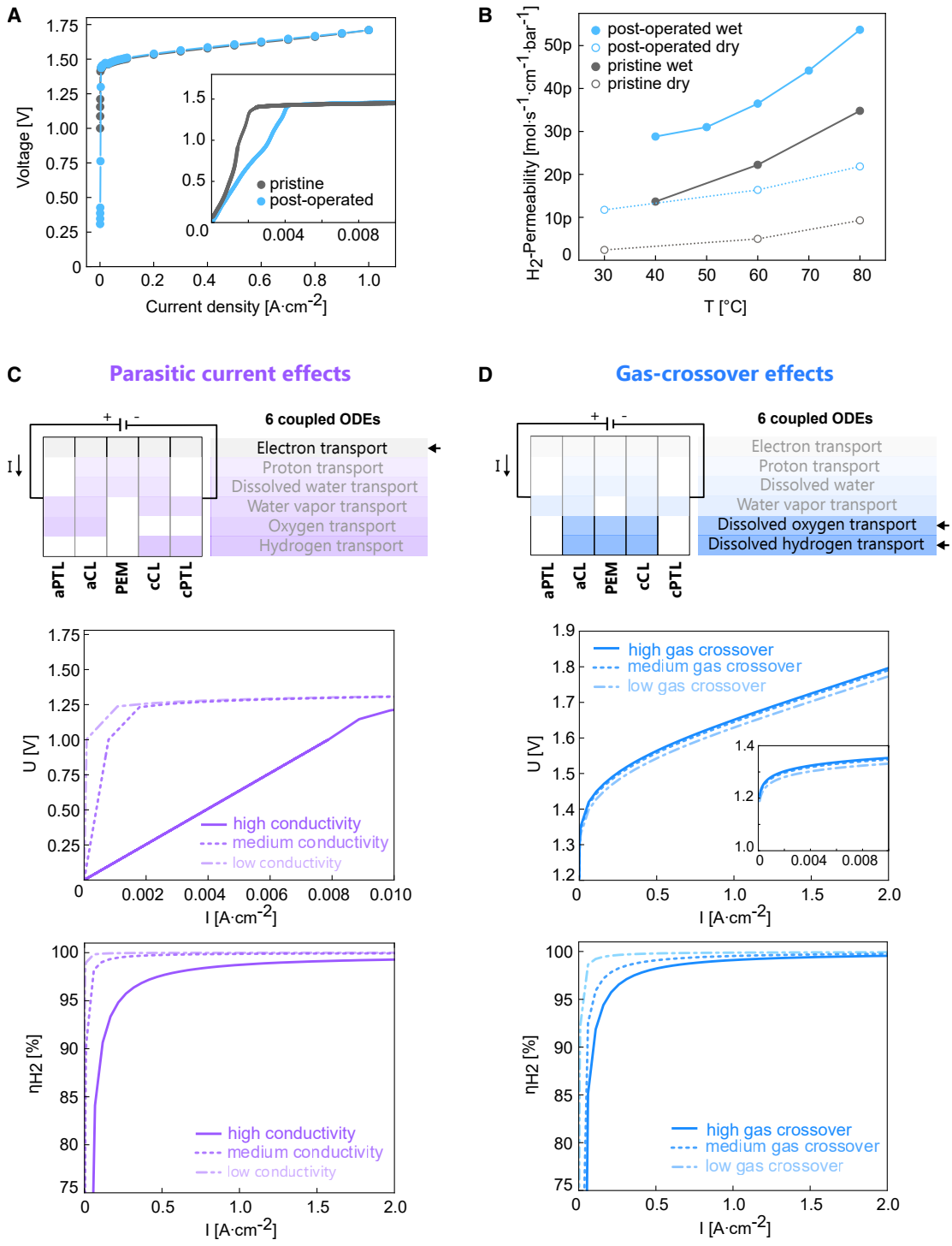

Figure 2. Experimental measurement and modeling of parasitic current and gas crossover

(A) Polarization curves of a pristine and post-operated MEA, including an inlet of the low current density range, indicating the existence of parasitic currents within the post-operated MEA.

(B) Hydrogen gas permeabilities of a pristine and post-operated MEA under wet and dry conditions.

(C and D) Results of computational modeling of parasitic current and gas-crossover effects in the MEA. On the top, the mathematical modeling assumptions for both parasitic electrical current and gas-crossover effects are presented. The polarization behavior and the Faradaic efficiency of hydrogen are plotted at the bottom of the figure. The parameters used for conductivity and gas crossover modeling can be found in Table S1.

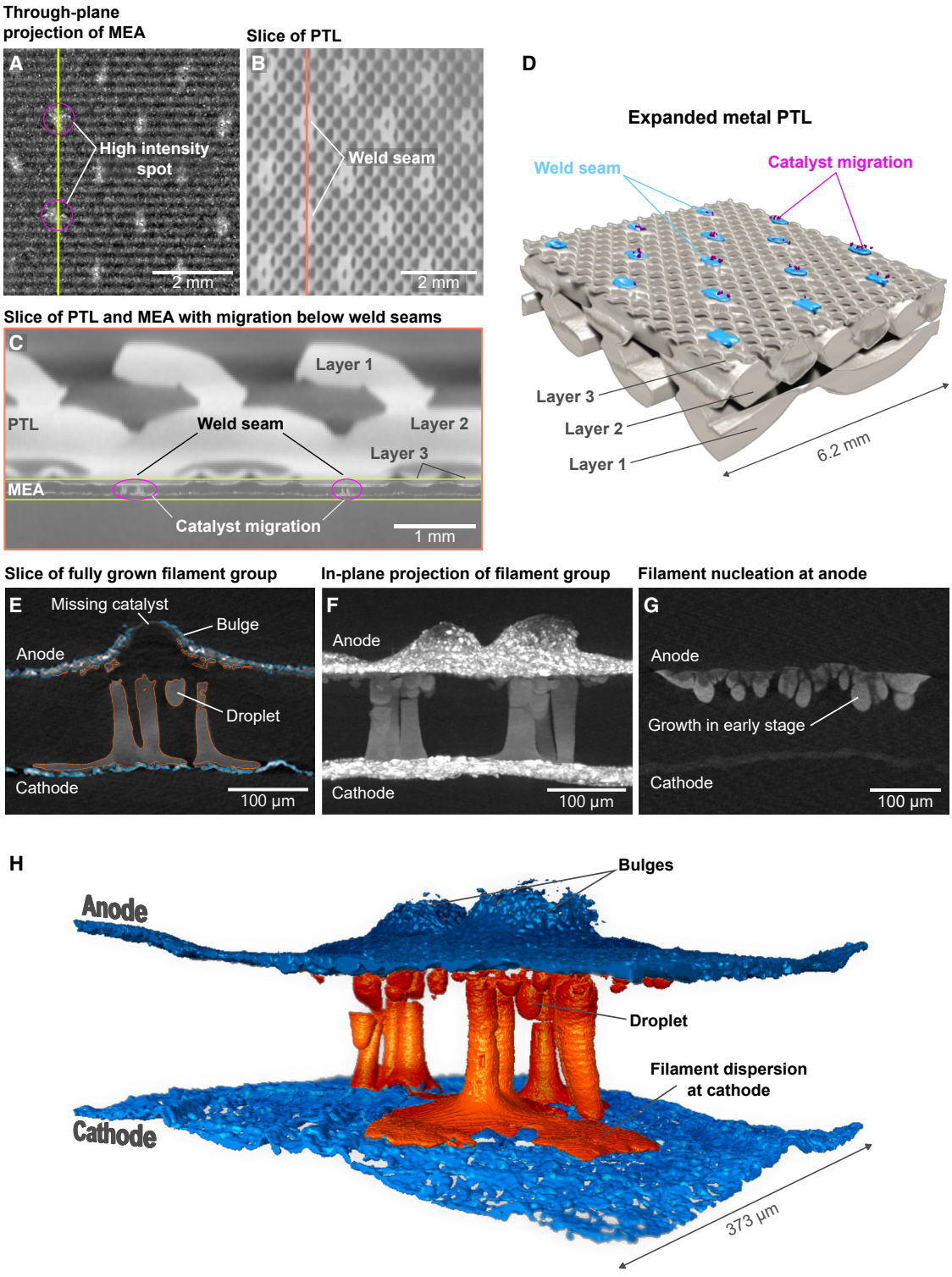

Figure 3. Filament discovery through XCT

(A) Through-plane projection of a low-resolution overview XCT scan, including spots of high-intensity voxels spaced approximately 2 mm apart.

(B) XCT slice of an exemplary expanded metal PTL showcasing the weld seams between layers 2 and 3 of the PTL.[38]

(C) Orthogonal view of two aligned XCT datasets showing the MEA (yellow box) and the PTL (orange box). Pink circles indicate filament groups aligned with the PTL weld seams.

(D) 3D visualization of the exemplary expanded metal PTL depicting the spatial locations of filament groups (pink) and weld seams (blue).

(legend continued on next page)

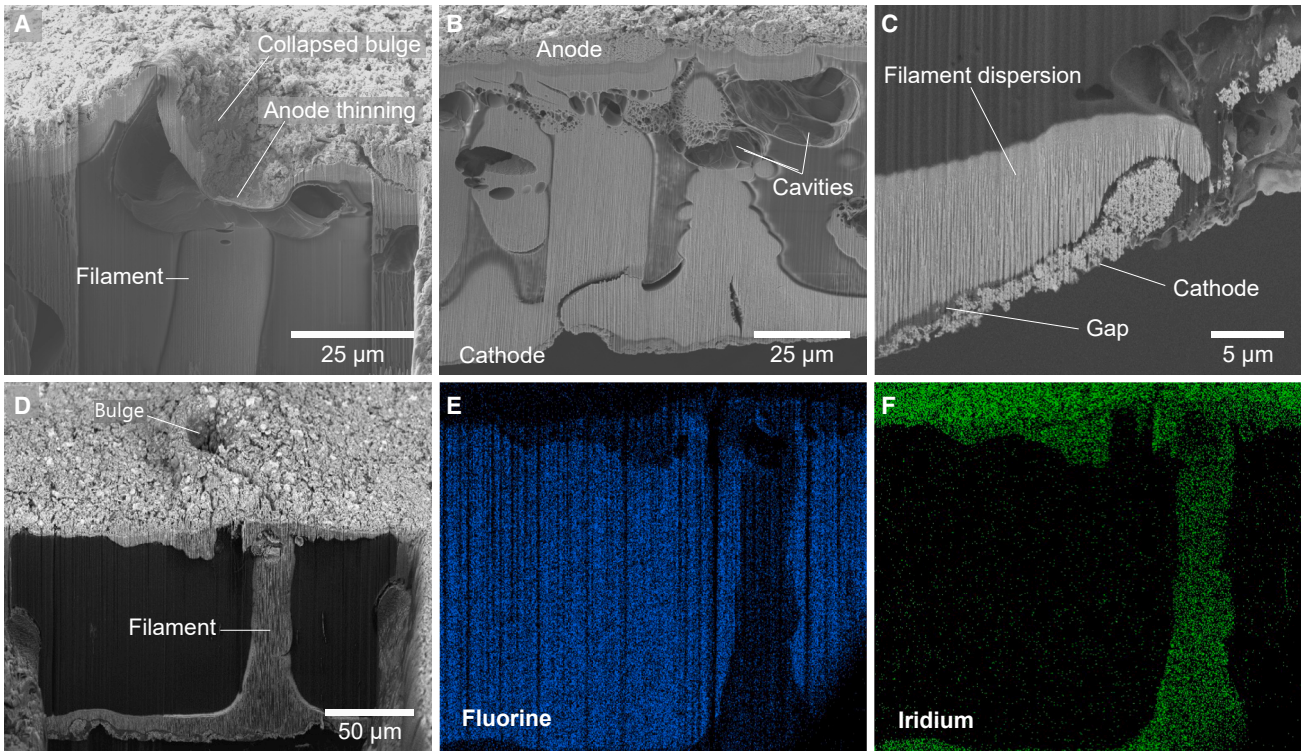

Figure 4. Filament analysis by FIB-SEM

(A) FIB-SEM cross-section of a bulge and filament, revealing a large cavity directly beneath the bulge. The bulge collapsed due to the drying of the MEA, which was necessary for the FIB slicing. The collapsed top of the bulge shows anode thinning.

(B) Complete cross-section from anode to cathode showing a group of filaments and numerous cavities close to the anode.

(C) Close-up of a cross-section showing filament dispersion at the cathode, revealing a visible gap between the filament and CL.

(D) Cross-section with a filament and corresponding bulge on the anode above it, prepared for EDS.

(E and F) EDS maps from the cross-section shown in (D), depicting signals of fluorine (blue) and iridium (green).

hypothesis that growth initiates at the anode and progresses toward the cathode over time. Importantly, the formation of filaments was observed across multiple system scales, and we were able to reproduce it several times under accelerated stress conditions (1,400 h; see Figures 8 and S2). Therefore, we conclude that filament growth is primarily driven by local interface design and electrochemical conditions, rather than cell size or custom materials, and may thus represent a general degradation mechanism in PEMECs.

Building upon the XCT findings and to characterize the microstructure of the filaments in more detail, a comprehensive investigation was initiated by combining focused ion beam scanning electron microscopy (FIB-SEM) with energy-dispersive X-ray spectroscopy (EDS). SEM images of the anode (Figure S3) reveal a noticeable contrast between the bulges and their surrounding area, attributed to material differences.[40] EDS analyses of the iridium catalyst at the same area detect signals of fluorine, a key component of the membrane (Figure S4), supporting the XCT observation that the membrane is exposed at the top of the bulges. Cross-sections of the filaments were prepared by milling the MEA with FIB at positions mapped by XCT. Figure 4A depicts a cross-section of a bulge that collapsed during preparation due to the drying of the MEA. A filament and a large cavity beneath the bulge, as well as a thinning of the anode, are visible. A full cross-section from anode to cathode is shown in Figure 4B, revealing a filament cluster and additional cavities of various sizes. A crack within a filament is visible, presumably caused either by stress introduced during the FIB-SEM sample preparation or by high local currents flowing through the small filament area, which could wear the material down over time. Noticeably, the filament dispersion is separated from the cathode by a small sub-micrometer gap (Figure 4C). To identify the elemental composition of the filaments, EDS mapping was performed on a cross-section (Figure 4D). The measurements

(E) Slice of a high-resolution tomogram showing the formation of filaments within the membrane and a bulge above, where the anode catalyst material is missing on the top.

(F) Projection of the maximal intensity of all slices from the tomogram shown in (E), showcasing a group of filaments and two bulges above them.

(G) XCT slice of an MEA operated with a shorter runtime of 1,200 h showing the nucleation of filaments at the anode in the early stages.

(H) Three-dimensional visualization of the segmented XCT data shown in (E) and (F).

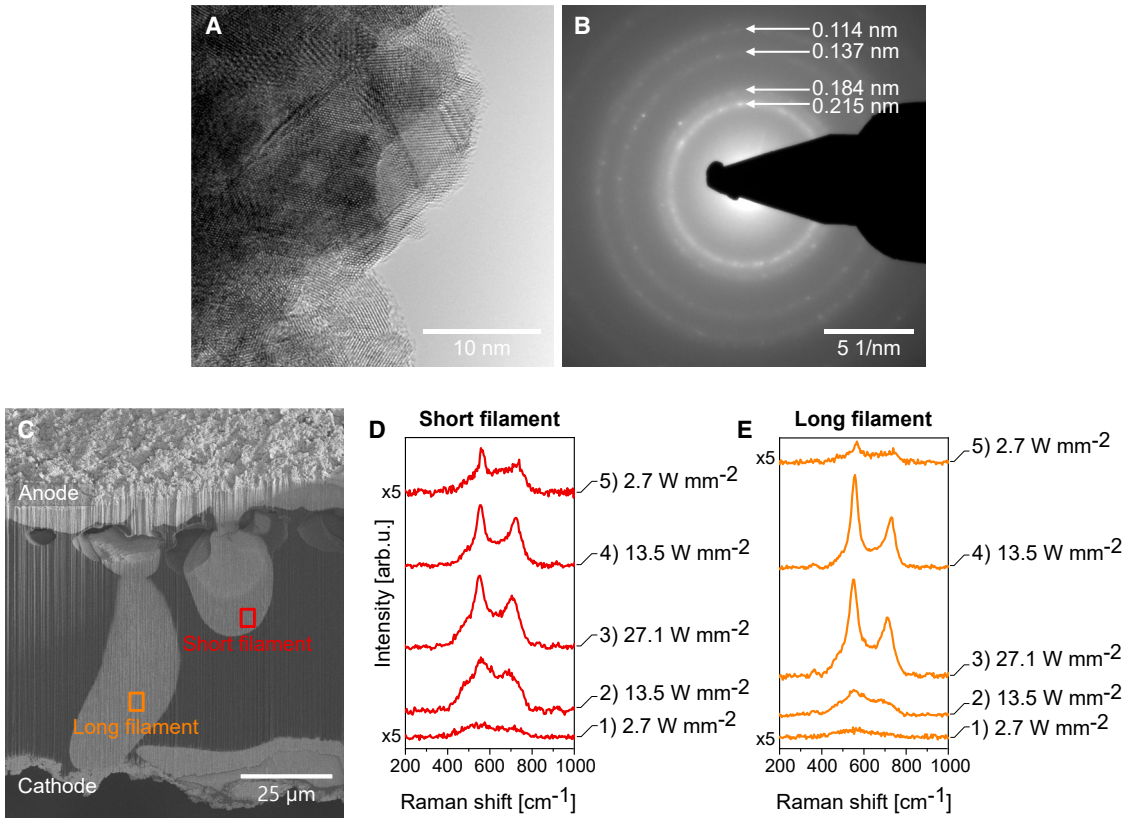

Figure 5. Filament composition analysis via TEM and Raman spectroscopy

(A) HRTEM image of a filament lamella depicting the crystalline nature of the material.

(B) SAED pattern of a filament lamella resembling close characteristics of iridium metal, indicating that nanocrystalline iridium is the major component of the filament.

(C) Cross-sectional SEM image of filaments depicting the measurement points at which the laser was focused during Raman spectroscopy.

(D and E) Raman spectra of the short (D) and long (E) filament pre- and post-thermal oxidation. Iridium oxide signals are only noticeable after thermal oxidation by laser in both filaments, verifying that the filaments mostly consist of nanocrystalline iridium rather than iridium oxide. The numbers 1–5 correspond to the increase and subsequent decrease of the laser power used for thermal oxidation.

indicate that the filaments are primarily composed of iridium, as shown by the EDS maps in Figures 4E and 4F.

Filament composition

While EDS can detect elemental composition, it cannot distinguish between crystalline iridium and its various oxides. To conclusively differentiate between the two, transmission electron microscopy (TEM) and Raman spectroscopy were applied.

For TEM analysis of the filament composition, a lamella of the MEA was prepared under cryogenic conditions using a xenon plasma-FIB. A low-magnification, high-angle annular dark-field scanning transmission electron microscopy (HAADF STEM) image, coupled with EDS (see Figure S5), verifies the filament material as an iridium phase embedded in polymer. To identify the specific iridium phase and assess its crystallinity, high-resolution TEM (HRTEM) and selected area electron diffraction (SAED) analyses were conducted. Figure 5A shows the HRTEM image of lattice fringes in a filament lamella, from which the d-spacing can be measured. Across various regions of the lamella, a consistent d-spacing of 0.214 nm was observed, corresponding to the first diffraction ring in the SAED pattern shown in Figure 5B. This d-spacing is assigned to the (111) plane of crystalline iridium. A comparison of the obtained diffraction pattern with simulated reflexes for iridium and iridium oxide (Figures S6 and S7) validates that the filaments consist of mostly nanocrystalline iridium rather than its oxide.

To validate the TEM results, Raman spectroscopy was applied. While iridium itself is Raman inactive, it can be oxidized and rendered detectable through thermal treatment, which occurs when the laser power is increased during measurement.[41] Raman spectra were collected from a short, partially developed filament and a long filament extending from anode to cathode (Figure 5C). Initially, with a low, non-oxidizing laser power of 2.7 W mm^{-2}, both filaments exhibit a weak and broad signal around 600 cm^{-1}. This low signal-to-noise ratio indicates that the filament surface contains only a small percentage of Raman-active material, supporting the TEM-based finding of the crystalline nature of the iridium filaments. When increasing the laser power, distinct signals for E_g (550 cm^{-1}), A_{1g}, and B_{2g} (710 cm^{-1}) bands appear. These bands persist even after the laser power is reduced again, indicating that iridium oxide was formed through thermal oxidation. While this behavior is observed in both the

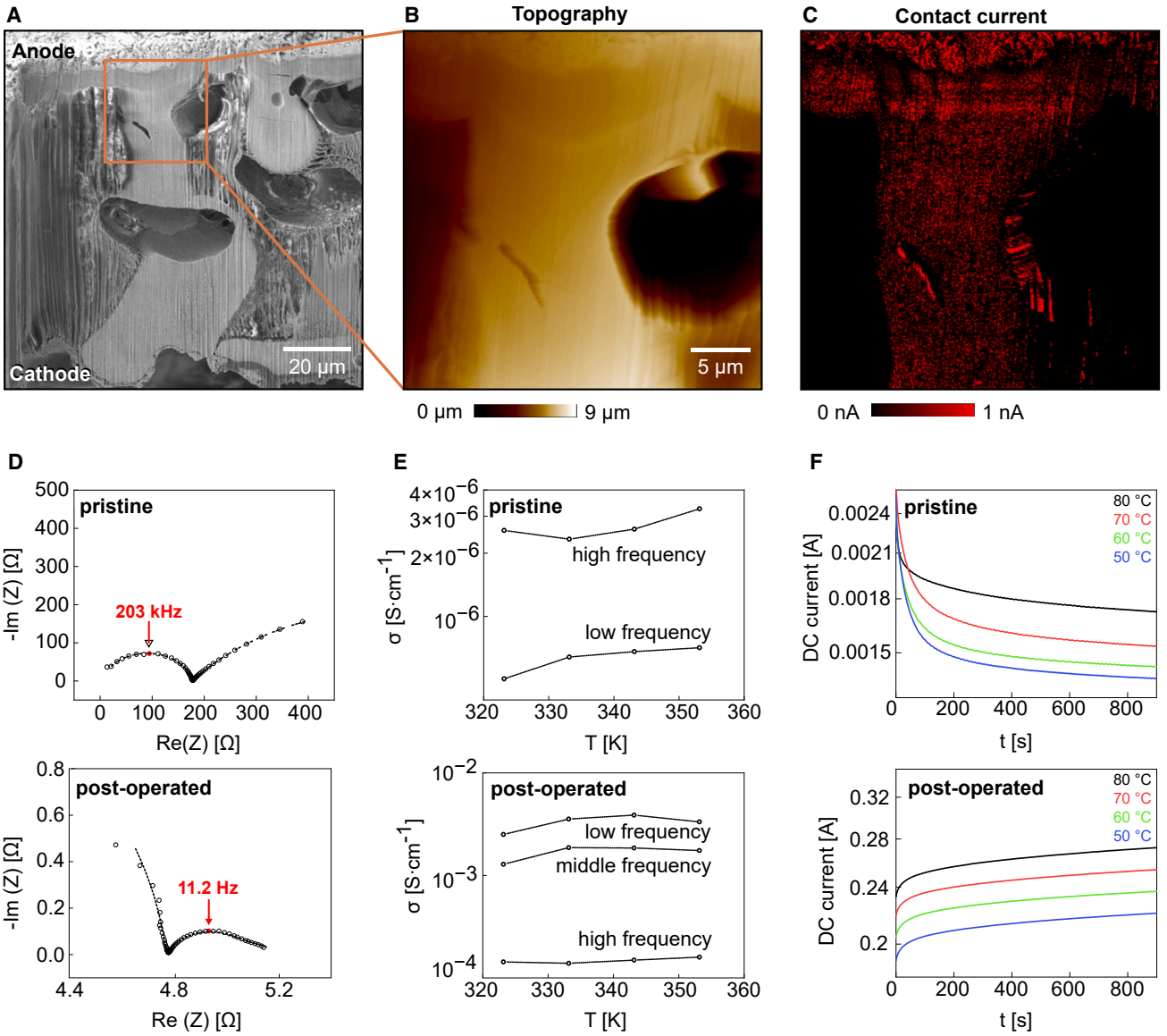

Figure 6. Filament conductivity measurements by current-sensing AFM and EIS

(A) FIB-SEM cross-section of a filament within a post-operated MEA, with the AFM scan area highlighted by an orange box.

(B) The AFM topography of the scanned area in (A) exhibits the same features, such as the crack in the filament or the cavity to the right.

(C) The corresponding contact current map to (B) clearly shows the electrically conductive nature of the filament.

(D) Nyquist graphs (imaginary vs. real impedance Z) of pristine (top) and post-operated (bottom) dried MEAs from through-plane measurements at 80°C under dry nitrogen flow. The MEAs were deliberately dried to eliminate proton conduction and obtain insights into electron conduction. The dashed lines indicate ECM fits. The critical characteristic frequencies are marked in red.

(E) Temperature dependence of the different conductivity contributions of pristine (top) and post-operated (bottom) MEAs (through-plane).

(F) Through-plane DC current of pristine (top) and post-operated (bottom) MEAs at 1 V DC voltage for different temperatures.

short and long filaments, differences are evident when comparing the linewidths of the iridium signals. At 2.7 W mm^{-2}, after oxidation, the increased contribution of sharp signals in the short filament indicates a higher degree of long-range order induced by thermal treatment. Thus, the long filament exhibited a distinct oxidation behavior compared with the short filament, despite having overall similar oxidation rates.

Filament conductivity

With the information gained that the filaments consist of mostly nanocrystalline iridium, their electrical properties were further investigated using current-sensing atomic force microscopy (AFM) (Figures 6A–6C). The contact current map (Figure 6C) reveals electron percolation paths persisting along the filament, clearly confirming its electrical conductivity. As expected, the

proton-conductive membrane surrounding the filament is electrically non-conductive.

The effect of this microscopic behavior on the macroscopic conductivity properties was ascertained by electrochemical impedance spectroscopy (EIS). To decouple the proton conduction of the membrane from electronic conduction pathways provided by the filament structures, the membrane was thoroughly dried by continuously supplying dry nitrogen gas. The Nyquist plots of the impedance spectra are depicted in Figure 6D. They pertain to both pristine and post-operated MEAs and were obtained after a 1-week drying period at a temperature of 80°C. To identify and attribute impedance processes occurring inside the cell without using complex physical models, equivalent circuit models (ECMs) are frequently employed. However, using a suitable model requires prior understanding of the system, and for PEM MEAs, no generally accepted ECM is available in the literature. Therefore, to choose an effective ECM for the complex system at hand, distribution of relaxation times (DRT) analysis was used[42] (Figures S8 and S9 and Note S1). The DRT method deconvolutes each electrochemical process into its characteristic time constant, thereby revealing the number of ECM components that are supported by the experimental data[43] (Figure S10). For additional context, more information about the DRT analysis can be found in the supplemental information Note S2.

The conductivity calculated from the low-frequency and high-frequency impedance data for the pristine MEA are 7.02×10^{-7} and 3.25×10^{-6} S/cm, respectively. The computed values are comparable to the values reported in the literature for dry Nafion 117.[44,45] For the post-operated MEA, the calculated conductivities are 1.59×10^{-4}, 1.75×10^{-3}, and 3.33×10^{-3} S/cm. This suggests that the presence of filaments has locally raised the conductivity by three orders of magnitude compared with the pristine state. However, this comparison is influenced by the change of local distances between PEM-separated conducting structures. By contrast, the 1D model shown in Figure 2C assumes a uniform conductivity increase across the membrane and predicts a much steeper voltage slope in the low current density regime at just two orders of magnitude higher conductivity. This discrepancy arises because the model does not capture the highly localized nature of the filaments that is measured in the EIS/DRT analysis. From the temperature dependency of the conductivity (Figure 6E), a qualitatively different behavior was observed from the pristine to the post-operated MEA, in particular for the high-frequency components. This indicates at least some changes of material properties. Potentiostatic DC measurements (Figure 6F) show that, while for both samples the DC current declines with decreasing temperature, the decline is linear for the post-operated MEA. For the pristine MEA, a more complicated trend can be seen, with a qualitative change at 80°C. As a general observation, the post-operated MEA exhibited DC current approximately 100 times higher than the pristine one. By comparing the time-domain data of the pristine and the post-operated MEA, it is observed that the response changes from a capacitive behavior, with decreasing current as a function of time, to an inductive behavior with an increase of current. This suggests a qualitative change of membrane properties for the post-operated MEA, indicating aging, i.e., chemical or mechanical changes of the membrane. Such a change is also implied by the change of the time constants obtained from ECM fits (Table S2).

Proposed filament growth mechanism

The preceding sections have provided an in-depth analysis of our experimental and computational data. Based on these insights, we propose the following mechanism, delineating our understanding of the filament growth within the PEMEC membrane.

Given that the filaments originate from the weld seam positions on the PTL, it is likely that the weld seams play a significant role in filament nucleation. As described earlier, weld seams in the expanded metal meshes can lead to a non-uniform MEA/PTL interface. This mechanical inhomogeneity could cause local electrical field enhancement and higher current density at this interface, resulting in increased catalytic activity compared with areas not directly in contact with the weld seams of the PTL. A dedicated model of the protonic potential (Figure S11) supports this assumption, showing a locally elevated potential region directly beneath a PTL weld seam, consistent with the suspected localized current concentration and enhanced reaction activity at these sites. In addition, a thermographic measurement of an MEA containing filaments (Figure S12) reveals localized hotspots that spatially coincide with filament clusters, confirming the presence of locally increased current density and Joule heating. Such enhanced catalytic behavior could further increase the water-splitting reaction, with iridium dissolution as a side reaction. During the catalytic cycle, iridium may dissolve as Ir^{3+}.[18,46] Simultaneously, dissolved oxygen may recombine to the gaseous phase inside the membrane and become trapped beneath the anode at weld seam positions due to limited mass transport (Figure 7A). Experimental oxygen permeability measurements (Figure S13) show that measurable oxygen permeation already occurs in pristine MEAs, indicating that oxygen transport through the membrane is intrinsic even before aging. Presumably, as oxygen accumulates, it eventually ruptures through the anode, causing bulges within it and leaving cavities in the membrane, increasing the surface area for Ir^{3+} to enter (Figure 7B). As the positively charged Ir^{3+} cations migrate toward the negatively charged cathode, H_2 consistently crosses over from the cathode to the anode through hydrophilic transport channels,[47,48] to a higher degree at the mechanically damaged positions underneath the weld seams. While the Ir^{3+} cations move toward the cathode, they are continuously reduced by the passing H_2, forming filaments primarily composed of nanocrystalline iridium (Figure 7C), which could exert localized mechanical stress, pushing the PFSA membrane aside during growth. The constant flow of hydrogen gas at the cathode/membrane interface forces Ir^{3+} cations to migrate laterally, leading to the dispersion of the filament and the sub-micrometer gap observed at the cathode's interface (Figure 7D). Although various migration paths of iridium into the membrane have been suggested on a laboratory scale before,[49–52] the systematic formation of mostly nanocrystalline Ir-filaments in direct correlation with the MEA/PTL interface has, however, not yet been observed before.

Conclusion

Using post-operated MEA samples derived from PEMECs in a realistic test field environment, this study documents a newly

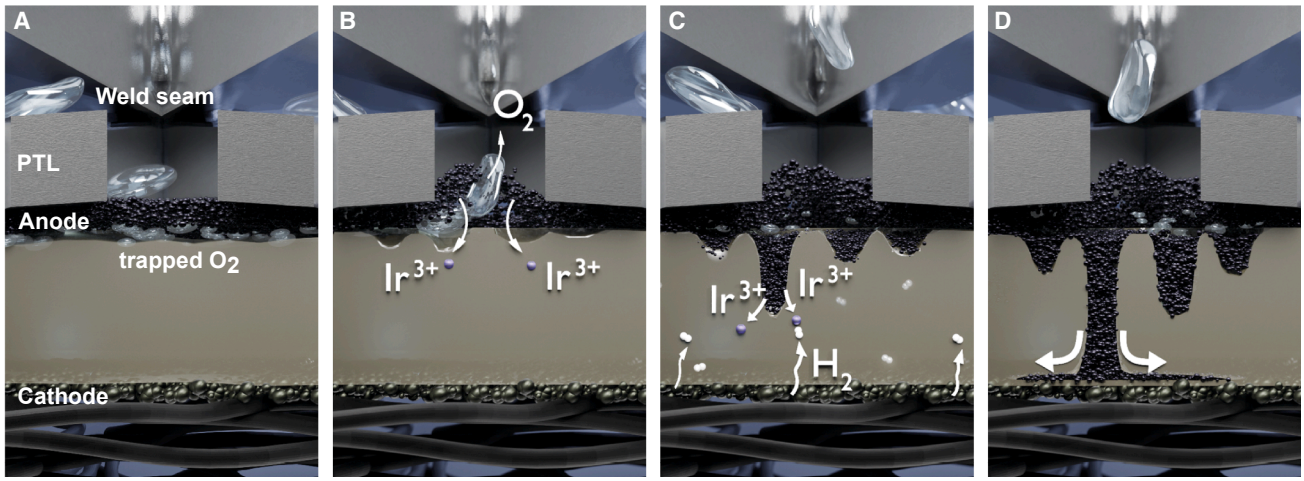

Figure 7. Schematic of the proposed filament growth mechanism

(A) Oxygen bubbles accumulate underneath the anode at weld seam positions due to limited mass transport.

(B) Presumably, O_2 ruptures through the anode, leading to bulges and mechanical damage within the membrane. Ir^{3+} migrates into the membrane and toward the cathode.

(C) The Ir^{3+} cations are reduced to metallic iridium by hydrogen that crosses over from cathode to anode, leading to the formation of iridium filaments.

(D) Finally, filaments disperse at the cathode, most likely due to high H_2 concentration at the interface.

discovered aging mechanism characterized by cross-plane formation of electrically conductive crystalline iridium filaments, triggered by the PTL/MEA interface design. Their growth is accompanied by a parasitic current flow through the membrane, which reduces local Faradaic efficiency and hydrogen yield, as demonstrated by our computational model. Complementary measurements confirmed increased gas crossover, posing additional safety risks for PEMEC operation after a certain threshold is reached.

We propose a growth mechanism for these filaments, starting with their nucleation at the anode, likely caused by a local increase in current density from the PTL weld seams. This triggers a side reaction of iridium dissolution, generating Ir^{3+} cations that migrate toward the cathode, during which they are continuously reduced to nanocrystalline iridium via H_2 crossover.

Thus, optimizing the design of PEMEC systems to improve current density distribution at the MEA is key to increasing their lifetime. Such optimizations, supported by in-depth analytics of PEMEC components exposed to realistic operation conditions for relevant runtimes, are crucial for an accelerated market ramp-up of PEMECs. Ultimately, this gained knowledge will help to bolster the lifetime and performance as well as mitigate degradation of PEMECs.

METHODS

Operation of the MEAs

Operation test field environment

The investigated MEAs consist of a web-reinforced PFSA membrane with an iridium-based anode and a platinum-based cathode, with both catalysts applied at a standard loading in the milligram range (no ultra-low loading). CLs were deposited via a decal transfer process, commonly used for consistent and precise application.[53] An application-relevant test profile of 5,000 h of operation with a randomized arbitrary profile influenced by the availability of low-cost electricity, including 155 start-stop cycles with different hardness, was applied to closely replicate realistic industrial conditions for PEM electrolysis applications. Operation was stopped when the average cell voltage approached approximately 1.8 V to obtain well-performing samples for analysis. Such a strategy is important for interpretation, because otherwise any observed change in, i.e., morphology, would be attributed to aging. During operation, a welded titanium expanded metal was applied as PTL at the anode. No additional microporous layer (MPL) was used.

Operation on a small laboratory scale

Laboratory-scale single-cell experiments were conducted on a Nafion N115-based MEA from purchased Ion Power GmbH, featuring a specified catalyst loading of 0.3 mg/cm^2 of platinum on the cathode and 1.0 mg/cm^2 of IrOx on the anode, with an active area of 4.4 $\times$ 4.4 cm^2. The load and voltage profile over the 1,400-h operation is shown in Figure 8. During operation, a welded titanium expanded metal was applied as PTL at the anode. No additional MPL was used. An accelerated stress test (AST) was performed on the MEAs, with a voltage upper limit of 3 V. Initially, a current density of 5.17 A/cm^2 was applied, followed by a reduction to 2.58 A/cm^2, and later increased again to 3.87 A/cm^2. The flow rate was 12 mL/min/cm^2. As shown in Figure 8, the MEA began exhibiting current limitations toward the end of the 1,400-h test. At this stage, measurable parasitic current also emerged, indicating possible degradation.

Polarization curves

The experiments to assess polarization curves under humidified conditions extend the conditioning process introduced by Wang et al.[54] During the conditioning in the galvanostatic mode, the current density was increased stepwise from 0.5 to 2 A/cm^2

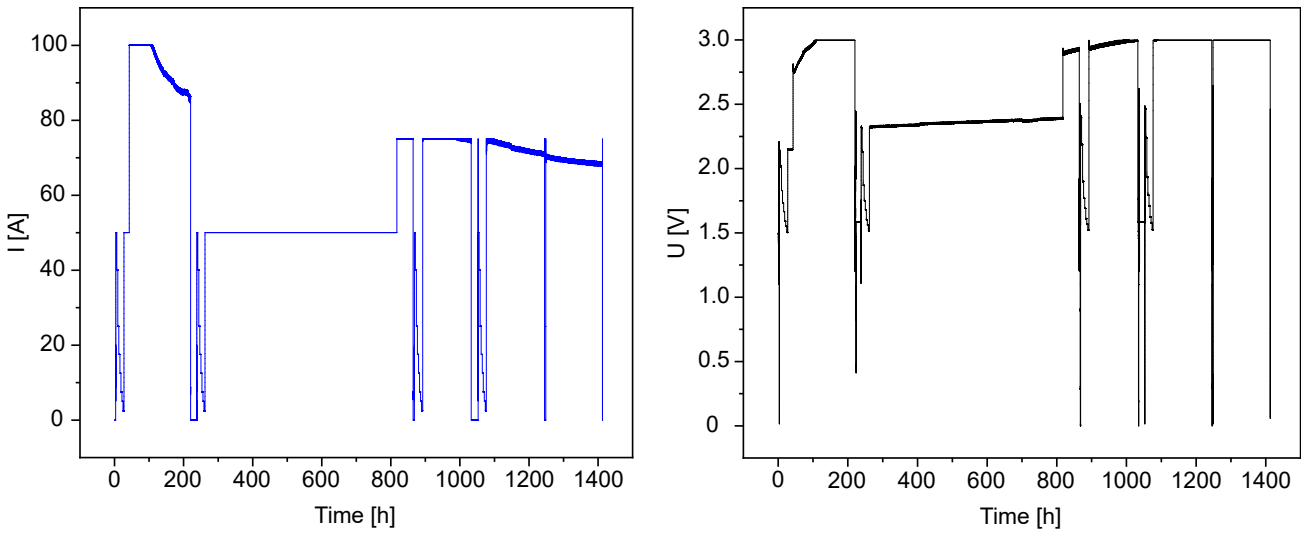

Figure 8. Applied current profile and corresponding potential of the laboratory-scale experiment

over approximately 15 h. For the polarization curves, 30 individual current densities were maintained for 1 min each, with voltage measurements taken once per second. Only the data points from the last 30 s of each step were used for analysis. The temperature was kept at 60°C throughout the experiment, and the flow rate of the deionized water on both the anode and cathode sides was 0.541 mL/min/cm^2.

Gas permeation

To determine the hydrogen gas permeability of the MEAs in the pristine and post-operated state, a setup similar to those already described in literature was used.[31,55–59] In this setup, the carrier gas (Ar, 6.0) was continuously flushed at a known flow rate at the opposite side of the permeate gas, regulated by a Bronkhorst F-201CV mass flow controller (MFC). Simultaneously, the permeate gas (H_2 or O_2, 6.0) was flushed at a known flow rate at the anode or cathode side accordingly, controlled by a Sensirion SFC5500 MFC. To keep the MEAs hydrated during measurements, both gases were humidified up to 100% relative humidity (RH) at 85°C, leading to the condensation of liquid water on the samples. The humidity of the gas was removed by cooling the mixture of permeate and carrier gas to 2°C when exiting the measurement cell, since the gas analyzer requires dry gas. To measure H_2 in Ar or O_2 in Ar in ppm, the gas mixture was analyzed using the thermal conductivity detector FTC320 by Messkonzept. The volume flow of the permeate was calculated from the known carrier gas flow $\dot{V}_{Ar}$ and the ratio of H_2 in Ar $R_{H2/Ar}$ in percent as follows:

$$\dot{V}_{H2} = \frac{R_{H2/Ar} \cdot \dot{V}_{Ar}}{1 - R_{H2/Ar}}. \qquad \text{(Equation 1)}$$

The cell used for the pretreatment and measurement of the MEAs is an in-house-built electrolysis cell with a square cell area of 18.49 cm^2. At the anode side, Pt-coated titanium was used as a flow field and titanium fiber as a gas diffusion layer (GDL). At the cathode, an Au-coated titanium flow field was utilized, whereas the PTL consisted of Toray Carbon Paper (TGP-H-60) and titanium wire mesh. For the measurement of the dry MEAs in the pristine and post-operated state, the MEAs were actively dried for 24 h at 80°C under a constant Ar flow of 100 mL/min on both the anode and cathode sides. The wet MEAs were humidified in deionized water at 80°C for 24 h. A film thickness gauge, type Käfer FD 1000/30-3, with an accuracy of 3 μm, was used to measure the thickness of all MEAs. Measurements were acquired at a pressure range of 5 to 1 bar, a carrier gas flow rate of 20 N mL/min, and a hydrogen flow rate of 50 N mL/min. Gas flow rates are reported in normal milliliters per minute (N mL/min), referenced to standard conditions (0°C and 1 atm).

Computational modeling

The high-aspect-ratio MEA lends itself to a 1D analysis. Here, two computational scenarios were taken into consideration. For each scenario, the mathematical model consists of a system of 1D steady ordinary differential equations (ODEs). The two systems of ODEs are briefly summarized in Figures 2C and 2D and describe stationary and isothermal transport processes occurring in the PTLs, CLs, and the PEM.[33–35] The electrochemistry model includes the charge balance equations for electrons and protons, the transport of water in ionomer, and the continuity equations for all gas species (e.g., H_2, O_2, and water vapor) in the system. Moreover, the reactions respect Butler-Volmer kinetics. O_2 and H_2 are produced due to the OER and hydrogen evolution reaction (HER), respectively. For the first scenario related to parasitic current effects (Figure 2C), the filaments are electron conductive, and electron transport can take place through them, whereas the gas species behave as ideal and do not permeate the PEM. For the second computational scenario related to gas-crossover effects (Figure 2D), the gas species are assumed to be dissolved in water within the ionomer phase and permeate through the post-operated MEAs. The material components of the MEA are supposed to be macroscopically homogeneous in the two scenarios. The two systems of ODEs

are entirely implemented in PYTHON and solved with the SOLVE_BVP solver from the submodule SCIPY.INTEGRATE, which is based on a fourth-order collocation method. Further details on the computational model and the mathematical framework, which serve as the basis, can be found in the recent work of Karyofylli et al.[60]

XCT

The first steps in the multi-modal imaging of the MEAs were taken by XCT. Here, the ZEISS XRADIA Versa 620 was employed, allowing for non-destructive imaging at a sub-micrometer scale. To prepare the samples for measurement, the post-operated MEAs were cut into 2 × 2 cm^2 pieces and then placed in a 1.5 mL centrifuge tube (Eppendorf) containing deionized water in a rolled-up position. This ensured the MEAs maintained a stable hydration state throughout the measurement process. A low magnification with a voxel size of approximately 13 μm was used to obtain an overall view of the sample. These low-resolution scans were conducted using an X-ray tube voltage of 40 kV. The tomograms were acquired using 1,600 projections over a 360° rotation with an exposure time of 3 s per projection.

Subsequently, a high-resolution scan with a voxel size of about 0.5 μm was performed to gain detailed insights into the electrodes and membrane. For this, the X-ray tube was set to 70 kV, providing sufficient photon flux to clearly delineate microscopic features. The high-resolved tomograms were obtained with 2,400 projections and an exposure time of 10 s each. For comparison, the pristine state of the MEA was also measured (see Figure S1). In addition to the MEAs, the PTL was measured *in vitro* at a low resolution with a voxel size of 25 μm, using a voltage of 100 kV. Here, a 360° scan with 1,600 projections and an exposure of 1 s was conducted. Finally, the post-processing and segmentation of all tomograms was performed with ImageJ[61] and Dragonfly software.[62]

FIB-SEM

Based on overview maps obtained from XCT marking the location of filaments, cross-sections or top-view images of the MEAs were acquired using either the Thermo Fisher Systems (TFS) Helios NanoLab 460F1 dual-beam FIB-SEM or the Tescan Amber X FIB-SEM. For imaging with the TFS Helios NanoLab 460F1, an ion conversion and electron detector (ICE) was used. When using the Tescan Amber X system, an Everhart-Thornley (E-T) secondary electron detector was employed, with beam parameters set between 2 and 5 kV for acceleration voltage and a current of 300 pA. Cross-sectioning with the TFS system was performed with an initial setting of 30 kV and 21 nA, followed by a polishing step at 30 kV and 0.24 nA. Cross-sections prepared with the Tescan Amber X system began with 30 kV and 300 nA. The current was continuously reduced during polishing, with the final step performed at 30 kV and 0.3 nA.

Elemental analysis via EDS was conducted using the "Octane Super" detector manufactured by EDAX, mounted on the Tescan Amber X FIB-SEM. For EDS measurements, the beam parameters were adjusted to an acceleration voltage of 20 kV and a beam current between 300 pA and 1 nA to obtain significant counts in a limited time.

TEM

For TEM investigations, a novel cryo-workflow was applied to reduce beam-induced damage during TEM sample preparation. In this workflow, the MEA was first slush frozen in liquid nitrogen and then placed in a Tescan Amber X FIB-SEM using Leica VCT500 cryo-transfer. The system was equipped with a Leica cryo-stage, which was operated at −160°C. The region of interest was located by measuring the distance from the sample edge obtained by XCT and subsequently milling the desired part of the MEA until filaments were found. Then the stage was tilted to prepare a TEM lamella from the filament area using a cryo-lift-out process.

STEM-EDS mapping was performed in a TFS Titan G2 80-200 ChemiStem, equipped with a Super-X EDS unit at 200 kV. HRTEM images and SAED were obtained using a Cs-corrected TFS Titan at 300 kV. The typical d-spacing of IrO_2 and iridium metal was determined using ReciprOgraph software[63] with data from the Crystallography Open Database[64–70] (Figures S6 and S7).

Raman spectroscopy

Raman experiments were performed on a WITec Alpha 300 Raman microscope. Here, a 532 nm laser and a ZEISS EC Epiplan-Neofluar HD Dic 50×/0.8 objective were utilized. Spectra were recorded with 10 accumulations and an integration time of 20 s. For each measurement position, measurements with an increasing and subsequently decreasing laser power density were performed in the following order to induce thermal oxidation within the filaments: 2.7, 13.5, 27.1, 13.5, and 2.7 W/mm^2.

AFM

The AFM measurement was performed with a Dimension Icon by Bruker in the force-distance curve-based and current-sensing PeakForce Tunneling AFM mode (PF TUNA, Bruker). A PPP-NCSTPt tip from Nanosensors with an electrically conductive $PtIr_5$ coating on the silicon tip and a nominal spring constant of 7.4 N/m was individually calibrated. The FIB-polished cross-section was installed into an electrically conductive holder, applying a bias voltage of 20 mV to both anode and cathode, while the conductive tip functioned as a counter electrode. The scan was performed with a constant maximum normal load of 40 nN, a scan rate of 0.2 Hz, and a resolution of 256 × 256 pixels. The averaged current over the tip/sample contact duration during each tapping cycle was recorded. Finally, the scans were processed with Nanoscope Analysis v3.0 (Bruker).[71]

EIS

EIS testing was conducted on a custom-made single-cell PEM electrolyzer with an active area of 17.64 cm^2. The testing involved both alternating current (AC) and direct current (DC) methods and was performed using pristine and post-operated MEAs likewise. Both MEA samples were immersed in deionized water for 1 week and then subjected to a drying process at a temperature of 80°C for another week. This was achieved by passing a continuous stream of dry nitrogen gas (100 mL/min) through the samples, with the gas flow controlled using an adapted apparatus equipped with mass flow controllers. The

experiments were conducted in the following descending temperature order: 80°C, 70°C, 60°C, and 50°C. The data were recorded at each temperature setpoint after sample equilibration for a day under a constant dry nitrogen flow. The impedance data in the four-wire mode were measured using an applied DC potential of 0 V with an AC amplitude of 0.1 V. The measurements were performed throughout a frequency range spanning from 50 mHz to 1 MHz. Moreover, DC tests were conducted at a voltage of 1 V. The measurements were carried out in a dry environment using a Zahner potentiostat. The thickness of the dried MEAs was calculated from SEM cross-sections of the MEA. The pristine membrane showed a thickness of (103.5 ± 2.3) μm, whereas the aged membrane exhibited a thickness of (92.4 ± 4.6) μm. DRTs were calculated using a home-written function running on Octave 8.4.[72]

RESOURCE AVAILABILITY

Lead contact

Further information and requests for resources should be directed to and will be fulfilled by the lead contact, Christine Heume (ch.heume@fz-juelich.de).

Materials availability

This study did not generate new, unique materials.

Data and code availability

- Primary data and code used in this manuscript have been deposited to 10.26165/JUELICH-DATA/IMZWZM.
- All other data are available in the main text or the extended data.
- Any additional information required to reanalyze the data reported in this paper is available from the lead contact upon request.

ACKNOWLEDGMENTS

The authors gratefully acknowledge the financial support by the German Federal Ministry of Research, Technology and Space (BMFTR) within the H_2Giga project DERIEL (grant number 03HY122C). The authors thank Siemens Energy for providing the samples. The authors thank Sebastian Lehmann (Forschungszentrum Jülich GmbH, IET-1) for his assistance in creating schematics showcasing the growth mechanism of the filaments. We also extend our gratitude to Tobias Mehlkoph (Forschungszentrum Jülich GmbH, IET-1) for his technical support in the laboratory during the collection of SEM data. Finally, we would like to thank Mary-Joan Blümich for her helpful comments on this manuscript and for editing the first draft.

AUTHOR CONTRIBUTIONS

Conceptualization, C.H., E.J., A.K., G.S., and R.-A.E.; methodology, C.H., A.J., V.K., K.D., S.B., J.-P.P., Y.T., Y.R., L.R., N.W., S.S., S.J., L.T., J.B., L.D., S.M., J.G., E.J., A.K., and R.-A.E.; investigation, C.H., A.J., V.K., S.B., J.-P.P., Y.T., Y.R., L.R., N.W., S.S., L.T., J.B., and J.G.; visualization, C.H.; funding acquisition, P.G., G.S., and R.-A.E.; project administration, L.D., S.M., E.J., A.K., G.S., and R.-A.E.; supervision, E.J., A.K., R.-A.E., K.D., S.B., S.J., F.H., A.J., H.K., L.D., S.M., and G.S.; writing – original draft, C.H., A.K., and R.-A.E. with comments from authors; writing – review & editing, C.H., A.J., V.K., K.D., S.B., J.-P.P., Y.R., N.W., S.S., S.J., L.T., J.B., F.H., L.D., S.M., J.G., H.K., E.J., P.G., A.K., G.S., and R.-A.E.

DECLARATION OF INTERESTS

The authors declare no competing interests.

SUPPLEMENTAL INFORMATION

Supplemental information can be found online at https://doi.org/10.1016/j.joule.2025.102238.

Received: August 15, 2025
Revised: October 19, 2025
Accepted: November 12, 2025
Published: January 21, 2026

REFERENCES

1. International Energy Agency (IEA) (2023). Global Hydrogen Review 2023 (IEA).
2. Ayers, K., Danilovic, N., Ouimet, R., Carmo, M., Pivovar, B., and Bornstein, M. (2019). Perspectives on Low-Temperature Electrolysis and Potential for Renewable Hydrogen at Scale. Annu. Rev. Chem. Biomol. Eng. *10*, 219–239. https://doi.org/10.1146/annurev-chembioeng-060718-030241.
3. Odenweller, A., Ueckerdt, F., Nemet, G.F., Jensterle, M., and Luderer, G. (2022). Probabilistic feasibility space of scaling up green hydrogen supply. Nat. Energy *7*, 854–865. https://doi.org/10.1038/s41560-022-01097-4.
4. Karl, A., Jodat, E., Kungl, H., Dobrenizki, L., Schmid, G., Geskes, P., and Eichel, R.A. (2025). Water Electrolysis Facing the Gigawatt Challenge—Comprehensive De-Risking of Proton Exchange Membrane and Anion Exchange Membrane Electrolyser Technology. Electrochemical Science Adv. *5*, e202400041. https://doi.org/10.1002/elsa.202400041.
5. Javed, A., Wolf, N.L., Meyer, F., Treutlein, L., Kungl, H., Karl, A., Jodat, E., and Eichel, R.-A. (2025). Exploring the state-of-operation of proton exchange membrane electrolyzers. Int. J. Hydrog. Energy *98*, 280–294. https://doi.org/10.1016/j.ijhydene.2024.12.055.
6. Turner, J.A. (2004). Sustainable Hydrogen Production. Science *305*, 972–974. https://doi.org/10.1126/science.1103197.
7. Pivovar, B., Rustagi, N., and Satyapal, S. (2018). Hydrogen at Scale (H_2 @Scale): Key to a Clean, Economic, and Sustainable Energy System. Electrochem. Soc. Interface *27*, 47–52. https://doi.org/10.1149/2.F04181if.
8. Lee, J.K., Babbe, F., Wang, G., Tricker, A.W., Mukundan, R., Weber, A.Z., and Peng, X. (2024). Nanochannel electrodes facilitating interfacial transport for PEM water electrolysis. Joule *8*, 2357–2373. https://doi.org/10.1016/j.joule.2024.06.005.
9. Xu, J., Jin, H., Lu, T., Li, J., Liu, Y., Davey, K., Zheng, Y., and Qiao, S.-Z. (2023). $IrO_x \cdot n\ H_2O$ with lattice water–assisted oxygen exchange for high-performance proton exchange membrane water electrolyzers. Sci. Adv. *9*, eadh1718. https://doi.org/10.1126/sciadv.adh1718.
10. Verbund Energy4Business GmbH. (2017), H2Future. https://cordis.europa.eu/project/id/735503.
11. WUN-H2. (2024). https://www.wun-h2.de/.
12. Engel, S.N.T.S. (2024). Regelfähigkeit von Elektrolyseanlagen (TenneT). https://netztransparenz.tennet.eu/fileadmin/user_upload/The_Electricity_Market/German_Market/Grid_customers/Kundenforum_2021/4_Kundenforum_30_11_21_Vortrag_Regelfaehigkeit_Elektrolyse.pdf.
13. Tomić, A.Z., Pivac, I., and Barbir, F. (2023). A review of testing procedures for proton exchange membrane electrolyzer degradation. J. Power Sources *557*, 232569. https://doi.org/10.1016/j.jpowsour.2022.232569.
14. Weiß, A., Siebel, A., Bernt, M., Shen, T.-H., Tileli, V., and Gasteiger, H.A. (2019). Impact of Intermittent Operation on Lifetime and Performance of a PEM Water Electrolyzer. J. Electrochem. Soc. *166*, F487–F497. https://doi.org/10.1149/2.0421908jes.
15. Alia, S.M., Stariha, S., and Borup, R.L. (2019). Electrolyzer Durability at Low Catalyst Loading and with Dynamic Operation. J. Electrochem. Soc. *166*, F1164–F1172. https://doi.org/10.1149/2.0231915jes.
16. Binninger, T., Mohamed, R., Waltar, K., Fabbri, E., Levecque, P., Kötz, R., and Schmidt, T.J. (2015). Thermodynamic explanation of the universal correlation between oxygen evolution activity and corrosion of oxide catalysts. Sci. Rep. *5*, 12167. https://doi.org/10.1038/srep12167.

17. Spöri, C., Kwan, J.T.H., Bonakdarpour, A., Wilkinson, D.P., and Strasser, P. (2017). The Stability Challenges of Oxygen Evolving Catalysts: Towards a Common Fundamental Understanding and Mitigation of Catalyst Degradation. Angew. Chem. Int. Ed. *56*, 5994–6021. https://doi.org/10.1002/anie.201608601.

18. Kasian, O., Grote, J.P., Geiger, S., Cherevko, S., and Mayrhofer, K.J.J. (2018). The Common Intermediates of Oxygen Evolution and Dissolution Reactions during Water Electrolysis on Iridium. Angew. Chem. Int. Ed. *57*, 2488–2491. https://doi.org/10.1002/anie.201709652.

19. Reier, T., Nong, H.N., Teschner, D., Schlögl, R., and Strasser, P. (2017). Electrocatalytic Oxygen Evolution Reaction in Acidic Environments – Reaction Mechanisms and Catalysts. Adv. Energy Mater. *7*, 1601275. https://doi.org/10.1002/aenm.201601275.

20. Pfeifer, V., Jones, T.E., Velasco Vélez, J.J., Arrigo, R., Piccinin, S., Hävecker, M., Knop-Gericke, A., and Schlögl, R. (2017). In situ observation of reactive oxygen species forming on oxygen-evolving iridium surfaces. Chem. Sci. *8*, 2143–2149. https://doi.org/10.1039/C6SC04622C.

21. Chandesris, M., Médeau, V., Guillet, N., Chelghoum, S., Thoby, D., and Fouda-Onana, F. (2015). Membrane degradation in PEM water electrolyzer: Numerical modeling and experimental evidence of the influence of temperature and current density. Int. J. Hydrog. Energy *40*, 1353–1366. https://doi.org/10.1016/j.ijhydene.2014.11.111.

22. Grigoriev, S.A., Dzhus, K.A., Bessarabov, D.G., and Millet, P. (2014). Failure of PEM water electrolysis cells: Case study involving anode dissolution and membrane thinning. Int. J. Hydrog. Energy *39*, 20440–20446. https://doi.org/10.1016/j.ijhydene.2014.05.043.

23. H2Giga. (2025). Wasserstoff-Leitprojekte. https://www.wasserstoff-leitprojekte.de/lw_resource/datapool/systemfiles/elements/files/17DD578FD8010397E0637E695E86289B/live/document/H2Giga_booklet.pdf.

24. Cammarata, A., and Mastropasqua, L. (2023). Theoretical analysis of mixed open-circuit potential for high temperature electrochemical cells electrodes. Front. Energy Res. *11*, 1120343. https://doi.org/10.3389/fenrg.2023.1120343.

25. Lettenmeier, P., Wang, R., Abouatallah, R., Burggraf, F., Gago, A.S., and Friedrich, K.A. (2016). Coated Stainless Steel Bipolar Plates for Proton Exchange Membrane Electrolyzers. J. Electrochem. Soc. *163*, F3119–F3124. https://doi.org/10.1149/2.0141611jes.

26. Dang, J., Li, Y., Liu, B., Hu, S., Yang, F., and Ouyang, M. (2023). Design and economic analysis of high-pressure proton exchange membrane electrolysis for renewable energy storage. Int. J. Hydrog. Energy *48*, 10377–10393. https://doi.org/10.1016/j.ijhydene.2022.11.250.

27. Hemauer, J., Rehfeldt, S., Klein, H., and Peschel, A. (2023). Performance and cost modelling taking into account the uncertainties and sensitivities of current and next-generation PEM water electrolysis technology. Int. J. Hydrog. Energy *48*, 25619–25634. https://doi.org/10.1016/j.ijhydene.2023.03.050.

28. Klose, C., Saatkamp, T., Münchinger, A., Bohn, L., Titvinidze, G., Breitwieser, M., Kreuer, K.D., and Vierrath, S. (2020). All-Hydrocarbon MEA for PEM Water Electrolysis Combining Low Hydrogen Crossover and High Efficiency. Adv. Energy Mater. *10*, 1903995. https://doi.org/10.1002/aenm.201903995.

29. Badwal, S.P.S., Giddey, S., and Ciacchi, F.T. (2006). Hydrogen and oxygen generation with polymer electrolyte membrane (PEM)-based electrolytic technology. Ionics *12*, 7–14. https://doi.org/10.1007/s11581-006-0002-x.

30. Schalenbach, M., Hoefner, T., Paciok, P., Carmo, M., Lueke, W., and Stolten, D. (2015). Gas Permeation through Nafion. Part 1: Measurements. J. Phys. Chem. C *119*, 25145–25155. https://doi.org/10.1021/acs.jpcc.5b04155.

31. Kusoglu, A., and Weber, A.Z. (2017). New Insights into Perfluorinated Sulfonic-Acid Ionomers. Chem. Rev. *117*, 987–1104. https://doi.org/10.1021/acs.chemrev.6b00159.

32. Naudy, S., Collette, F., Thominette, F., Gebel, G., and Espuche, E. (2014). Influence of hygrothermal aging on the gas and water transport properties of Nafion® membranes. J. Membr. Sci. *451*, 293–304. https://doi.org/10.1016/j.memsci.2013.10.013.

33. García-Salaberri, P.A. (2022). 1D two-phase, non-isothermal modeling of a proton exchange membrane water electrolyzer: An optimization perspective. J. Power Sources *521*, 230915. https://doi.org/10.1016/j.jpowsour.2021.230915.

34. Trinke, P. (2021) Experimental and Model-Based Investigations on Gas Crossover in Polymer Electrolyte Membrane Water Electrolyzers. https://doi.org/10.15488/10979.

35. Franz, T., Papakonstantinou, G., and Sundmacher, K. (2023). Transient hydrogen crossover in dynamically operated PEM water electrolysis cells - A model-based analysis. J. Power Sources *559*, 232582. https://doi.org/10.1016/j.jpowsour.2022.232582.

36. Karyofylli, V., Raman, K.A., Hammacher, L., Danner, Y., Kungl, H., Karl, A., Jodat, E., and Eichel, R.A. (2025). Elucidating Parasitic Currents in Proton-Exchange-Membrane Electrolytic Cells via Physics-Based and Data-Driven Modeling. Electrochemical Science Adv. *5*, e70000. https://doi.org/10.1002/elsa.70000.

37. Schalenbach, M., Tjarks, G., Carmo, M., Lueke, W., Mueller, M., and Stolten, D. (2016). Acidic or Alkaline? Towards a New Perspective on the Efficiency of Water Electrolysis. J. Electrochem. Soc. *163*, F3197–F3208. https://doi.org/10.1149/2.0271611jes.

38. Stiber, S., Sata, N., Morawietz, T., Ansar, S.A., Jahnke, T., Lee, J.K., Bazylak, A., Fallisch, A., Gago, A.S., and Friedrich, K.A. (2022). A high-performance, durable and low-cost proton exchange membrane electrolyser with stainless steel components. Energy Environ. Sci. *15*, 109–122. https://doi.org/10.1039/D1EE02112E.

39. Kak, A.C., and Slaney, M. (2001). Principles of Computed Tomographic Imaging (SIAM).

40. Ul-Hamid, A. (2018). A Beginners' Guide to Scanning Electron Microscopy (Springer International Publishing). https://doi.org/10.1007/978-3-319-98482-7.

41. Speer, S., Jovanovic, S., Merlen, A., Bartoli, F., Kiran, K., Wolf, N., Karl, A., Jodat, E., and Eichel, R.-A. (2025). Laser induced oxidation Raman spectroscopy as an analysis tool for iridium-based oxygen evolution catalysts. Phys. Chem. Chem. Phys. *27*, 2570–2577. https://doi.org/10.1039/D4CP03592E.

42. Schichlein, H., Müller, A.C., Voigts, M., Krügel, A., and Ivers-Tiffée, E. (2002). Deconvolution of electrochemical impedance spectra for the identification of electrode reaction mechanisms in solid oxide fuel cells. J. Appl. Electrochem. *32*, 875–882. https://doi.org/10.1023/A:1020599525160.

43. Weiß, A., Schindler, S., Galbiati, S., Danzer, M.A., and Zeis, R. (2017). Distribution of Relaxation Times Analysis of High-Temperature PEM Fuel Cell Impedance Spectra. Electrochim. Acta *230*, 391–398. https://doi.org/10.1016/j.electacta.2017.02.011.

44. Mazzapioda, L., Navarra, M.A., Trequattrini, F., Paolone, A., Elamin, K., Martinelli, A., and Palumbo, O. (2019). Composite Nafion Membranes with CaTiO3−δ Additive for Possible Applications in Electrochemical Devices. Membranes *9*, 143. https://doi.org/10.3390/membranes9110143.

45. Di Noto, V., Piga, M., Pace, G., Negro, E., and Lavina, S. (2008). Dielectric Relaxations and Conductivity Mechanism of Nafion: Studies Based on Broadband Dielectric Spectroscopy. ECS Trans. *16*, 1183–1193. https://doi.org/10.1149/1.2981960.

46. Cherevko, S., Geiger, S., Kasian, O., Mingers, A., and Mayrhofer, K.J.J. (2016). Oxygen evolution activity and stability of iridium in acidic media. Part 1. – Metallic iridium. J. Electroanal. Chem. *773*, 69–78. https://doi.org/10.1016/j.jelechem.2016.04.033.

47. Dang, J., Zhang, J., Deng, X., Yang, S., Liu, B., Zhu, X., Li, Y., Yang, F., and Ouyang, M. (2023). Hydrogen crossover measurement and durability assessment of high-pressure proton exchange membrane electrolyzer. J. Power Sources *563*, 232776. https://doi.org/10.1016/j.jpowsour.2023.232776.

48. Schalenbach, M., Carmo, M., Fritz, D.L., Mergel, J., and Stolten, D. (2013). Pressurized PEM water electrolysis: Efficiency and gas crossover. Int. J. Hydrog. Energy *38*, 14921–14933. https://doi.org/10.1016/j.ijhydene.2013.09.013.

49. Zeng, Z., Ouimet, R., Bonville, L., Niedzwiecki, A., Capuano, C., Ayers, K., Soleymani, A.P., Jankovic, J., Yu, H., Mirshekari, G., et al. (2022). Degradation Mechanisms in Advanced MEAs for PEM Water Electrolyzers Fabricated by Reactive Spray Deposition Technology. J. Electrochem. Soc. *169*, 054536. https://doi.org/10.1149/1945-7111/ac7170.

50. Milosevic, M., Böhm, T., Körner, A., Bierling, M., Winkelmann, L., Ehelebe, K., Hutzler, A., Suermann, M., Thiele, S., and Cherevko, S. (2023). In Search of Lost Iridium: Quantification of Anode Catalyst Layer Dissolution in Proton Exchange Membrane Water Electrolyzers. ACS Energy Lett. *8*, 2682–2688. https://doi.org/10.1021/acsenergylett.3c00193.

51. Stähler, M., Burdzik, A., Friedrich, I., Everwand, A., and Scheepers, F. (2024). Oxygen flow rate measurement as a whistleblower for degradation effects in PEM water electrolysis. Int. J. Hydrog. Energy *78*, 682–687. https://doi.org/10.1016/j.ijhydene.2024.06.334.

52. Alia, S.M., Reeves, K.S., Cullen, D.A., Yu, H., Kropf, A.J., Kariuki, N., Park, J.H., and Myers, D.J. (2024). Simulated Start-Stop and the Impact of Catalyst Layer Redox on Degradation and Performance Loss in Low-Temperature Electrolysis. J. Electrochem. Soc. *171*, 044503. https://doi.org/10.1149/1945-7111/ad2bea.

53. Siemens, E. (2024). Electrolyzer Gigawatt Factory. https://www.siemens-energy.com/global/en/home/stories/electrolyzer-gigawatt-factory.html.

54. Wang, W., Li, K., Ding, L., Yu, S., Xie, Z., Cullen, D.A., Yu, H., Bender, G., Kang, Z., Wrubel, J.A., et al. (2022). Exploring the Impacts of Conditioning on Proton Exchange Membrane Electrolyzers by *In Situ* Visualization and Electrochemistry Characterization. ACS Appl. Mater. Interfaces *14*, 9002–9012. https://doi.org/10.1021/acsami.1c21849.

55. Kang, Z., Pak, M., and Bender, G. (2021). Introducing a novel technique for measuring hydrogen crossover in membrane-based electrochemical cells. Int. J. Hydrog. Energy *46*, 15161–15167. https://doi.org/10.1016/j.ijhydene.2021.02.054.

56. Yoshitake, M., Tamura, M., Yoshida, N., and Ishisaki, T. (1996). Studies of Perfluorinated Ion Exchange Membranes for Polymer Electrolyte Fuel Cells. Denki Kagaku1961 *64*, 727–736. https://doi.org/10.5796/kogyobutsurikagaku.64.727.

57. Sakai, T., Takenaka, H., and Torikai, E. (1986). Gas Diffusion in the Dried and Hydrated Nafions. J. Electrochem. Soc. *133*, 88–92. https://doi.org/10.1149/1.2108551.

58. Broka, K., and Ekdunge, P. (1997). Oxygen and hydrogen permeation properties and water uptake of Nafion® 117 membrane and recast film for PEM fuel cell. J. Appl. Electrochem. *27*, 117–123. https://doi.org/10.1023/A:1018469520562.

59. Arena, F., Mitzel, J., and Hempelmann, R. (2013). Permeability and Diffusivity Measurements on Polymer Electrolyte Membranes. Fuel Cells *13*, 58–64. https://doi.org/10.1002/fuce.201200116.

60. Karyofylli, V., Danner, Y., Ashoke Raman, K., Kungl, H., Karl, A., Jodat, E., and Eichel, R.-A. (2024). Sensitivity analysis and uncertainty quantification in predictive modeling of proton-exchange membrane electrolytic cells. J. Power Sources *600*, 234209. https://doi.org/10.1016/j.jpowsour.2024.234209.

61. Schneider, C.A., Rasband, W.S., and Eliceiri, K.W. (2012). NIH Image to ImageJ: 25 years of image analysis. Nat. Methods *9*, 671–675. https://doi.org/10.1038/nmeth.2089.

62. Dragonfly. (2022), [Version 2022.02] (Comet Technologies Canada Inc.).

63. Schoeni, N., and Chapuis, G. (2024) ReciprOgraph.

64. Downs, R.T., and Hall-Wallace, M. (2003). The American Mineralogist crystal structure database. Am. Mineral. *88*, 247–250.

65. Gražulis, S., Merkys, A., Vaitkus, A., and Okulič-Kazarinas, M. (2015). Computing stoichiometric molecular composition from crystal structures. J. Appl. Crystallogr. *48*, 85–91. https://doi.org/10.1107/S1600576714025904.

66. Gražulis, S., Daškevič, A., Merkys, A., Chateigner, D., Lutterotti, L., Quirós, M., Serebryanaya, N.R., Moeck, P., Downs, R.T., and Le Bail, A. (2012). Crystallography Open Database (COD): an open-access collection of crystal structures and platform for world-wide collaboration. Nucleic Acids Res. *40*, D420–D427. https://doi.org/10.1093/nar/gkr900.

67. Gražulis, S., Chateigner, D., Downs, R.T., Yokochi, A.F.T., Quirós, M., Lutterotti, L., Manakova, E., Butkus, J., Moeck, P., and Le Bail, A. (2009). Crystallography Open Database – an open-access collection of crystal structures. J. Appl. Crystallogr. *42*, 726–729. https://doi.org/10.1107/S0021889809016690.

68. Merkys, A., Vaitkus, A., Grybauskas, A., Konovalovas, A., Quirós, M., and Gražulis, S. (2023). Graph isomorphism-based algorithm for cross-checking chemical and crystallographic descriptions. J. Cheminform. *15*, 25. https://doi.org/10.1186/s13321-023-00692-1.

69. Quirós, M., Gražulis, S., Girdzijauskaitė, S., Merkys, A., and Vaitkus, A. (2018). Using SMILES strings for the description of chemical connectivity in the Crystallography Open Database. J. Cheminform. *10*, 23. https://doi.org/10.1186/s13321-018-0279-6.

70. Vaitkus, A., Merkys, A., and Gražulis, S. (2021). Validation of the Crystallography Open Database using the Crystallographic Information Framework. J. Appl. Crystallogr. *54*, 661–672. https://doi.org/10.1107/S1600576720016532.

71. Bruker. Nanoscope Analysis, [Version 3.00].

72. Eaton, J.W. (2002). Octave, [Version 8.3] (Network Theory Limited).